

## Distribution of porosity surrounding a microfiber in cement paste

He, Shan; Chen, Yu; Liang, Minfei; Yang, En-Hua; Schlangen, Erik

**DOI**

[10.1016/j.cemconcomp.2023.105188](https://doi.org/10.1016/j.cemconcomp.2023.105188)

**Publication date**

2023

**Document Version**

Final published version

**Published in**

Cement and Concrete Composites

**Citation (APA)**

He, S., Chen, Y., Liang, M., Yang, E.-H., & Schlangen, E. (2023). Distribution of porosity surrounding a microfiber in cement paste. *Cement and Concrete Composites*, 142, Article 105188. <https://doi.org/10.1016/j.cemconcomp.2023.105188>

**Important note**

To cite this publication, please use the final published version (if applicable). Please check the document version above.

**Copyright**

Other than for strictly personal use, it is not permitted to download, forward or distribute the text or part of it, without the consent of the author(s) and/or copyright holder(s), unless the work is under an open content license such as Creative Commons.

**Takedown policy**

Please contact us and provide details if you believe this document breaches copyrights. We will remove access to the work immediately and investigate your claim.



## Distribution of porosity surrounding a microfiber in cement paste

Shan He<sup>a,\*</sup>, Yu Chen<sup>a</sup>, Minfei Liang<sup>a</sup>, En-Hua Yang<sup>b</sup>, Erik Schlangen<sup>a</sup>

<sup>a</sup> *Microlab, Faculty of Civil Engineering and Geosciences, Delft University of Technology, Delft, 2628 CN, the Netherlands*

<sup>b</sup> *School of Civil and Environmental Engineering, Nanyang Technological University, Singapore, 639798, Singapore*

### ARTICLE INFO

#### Keywords:

Microstructure (B)  
Fiber reinforcement (E)  
Interfacial transition zone (B)  
Characterization (B)  
Nanoindentation

### ABSTRACT

This study investigates the microstructural changes of cement paste due to the inclusion of polymeric microfiber at different water-to-cement (w/c) ratios. A procedure to quantify the porosity of epoxy impregnated interfacial transition zone (ITZ) is also presented. Results show that the microstructures of the ITZ beneath and above a microfiber, with respect to the gravity direction, are largely different. Though the ITZ at both sides of the fiber are more porous than the bulk matrix, the porosity of the lower ITZ (*i.e.*, the ITZ beneath a fiber) is significantly higher than the upper side (*i.e.*, the ITZ above a fiber). This difference can be attributed to the combined effects of fiber on the initial packing of surrounding cement grains and on the settlement of the fresh mixture. The porosity gradients of the upper ITZs are found to be nearly identical for all the tested w/c ratios, while the porosity gradients of the lower ITZs become steeper when the w/c is higher. The lower side is also found to be the preferred location for the precipitation of calcium hydroxide crystals. Results of energy-dispersive X-ray spectroscopy (EDS) and nano-indentation analyses confirm that the chemical and mechanical properties of the ITZ are also asymmetric.

### 1. Introduction

The quasi-brittle nature of cement-based materials has caused poor performance of concrete in tension. Even at a low level of tensile stress, cracks can initiate and degrade concrete properties over time. Fiber reinforcement has, therefore, been used in concrete to overcome the brittleness and to extend its service life. Various types of fiber reinforcement, such as discrete or short (chopped) fiber [1], continuous or long (unidirectional) fiber [2], and woven fabric [3], have all been used in concrete. These fibers offer a wide scope to tailor a range of properties including post-cracking ductility [4,5], impact resistance [6], self-healing capability [7], and durability characteristics [8]. Among all the fibers, synthetic microfiber, such as polyvinyl alcohol (PVA) and polyethylene (PE) microfiber, have become increasingly popular for its effectiveness in crack width control as well as its resistance to harsh environment (*i.e.*, alkaline/acidic). One example of such polymeric microfiber reinforced cement-based composites is the strain hardening cementitious composite (SHCC), or engineered cementitious composite (ECC) [9], which has a typical tensile strain capacity exceeding 3% as a result of the formation of closely spaced microcracks with self-controlled crack width.

Among the various material parameters that influence the composite

properties, the interfacial bond between cement-based matrix and fiber is the most important. In terms of fracture resistance, it is essential to design fiber/matrix interfaces that can achieve high energy absorption through frictional sliding [10–12]. Ideally, the bond properties should not be too weak or too strong since poor bond properties can result in inefficient load and energy transfer between the matrix and fiber, while excessive bond can reduce the composite fracture energy due to fiber rupture. There is ample evidence that all composite properties beyond the linear elastic range of deformation may be linked to the failure of the fiber/matrix interface, if fiber rupture is prevented. Understanding the interaction between matrix and fiber is thus the key to improve the performance of microfiber reinforced cementitious composites.

Despite the importance of fiber/matrix bond properties, there remains a lack of comprehensive understanding of the microstructure of the interface/interphase between fiber and matrix. Although it is well documented that a distinct transition zone characterized by high porosity exists between bulk matrix and a big inclusion such as an aggregate [13–15] or a macrofiber [16,17], study of the microstructure of the interfacial transition zone (ITZ) between microfiber and cement-based matrix is still limited. Previous studies on the characterization of the microfiber/matrix ITZ also reported contradictory results. Based on scanning electron microscopy (SEM) examination, it has been

\* Corresponding author. Stevinweg 1, 2628 CN, Delft, the Netherlands.

E-mail address: [s.he-2@tudelft.nl](mailto:s.he-2@tudelft.nl) (S. He).

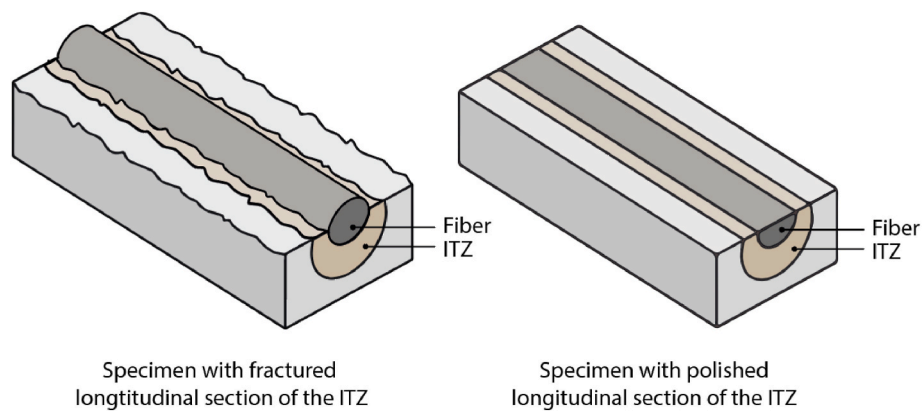


Fig. 1. Schematic illustration of 2 types of specimens used in the current study.

reported that cement-based matrices around a microfiber feature a dense microstructure and that no obvious transitional area can be observed, which contrasts with the studies investigating bigger inclusion, such as aggregates and macrofibers [15,18]. This has been attributed to the small diameter of microfibers, which is usually of the same order of magnitude as that of cement particles. Thus, the wall effect that gives rise to the formation of the ITZ may be largely minimized [19,20]. However, Chan and Li [12] reported that high porosity were indeed observed around a micro-PE fiber having a diameter of 38  $\mu\text{m}$  and showed that the porosity decreases when the water-to-cement ratio (w/c) is reduced. Xu et al. [16] also reported that capillary voids and low-density cement hydration products tend to prevail in the vicinity of polypropylene (PP) fiber surface, especially at a high w/c ratio. The volume fraction of voids in the ITZ between PP microfiber surface and the cement matrix was observed to increase from 22% to 25% and 43% when the w/c increased from 0.35 to 0.40 and 0.45. Recently, He et al. [21,22] reported that porous ITZ could still be observed even when the w/c of the matrix is as low as 0.2.

Disagreement among published literature on the subject matter may be due to three reasons. Firstly, microstructural observations made by SEM are often qualitative, and the determination of porosity can be subjective. Secondly, established methods of characterizing the ITZ around a microfiber often perform analyses on cross-sectional planes that are either perpendicular or intersect with the fiber axis at a random angle, which can lead to errors and uncertainties due to the heterogeneous nature of the ITZ microstructure. Lastly, the small diameter of the microfiber creates significant difficulties in sample preparation. These issues can contribute to the lack of consensus on the microstructure of the fiber/matrix interface, and highlight the need for more precise and reproducible methods of characterization to improve our understanding of the ITZ and its effect on composite properties.

To address the issues mentioned above, this paper quantitatively investigated the microstructure of the ITZ between microfiber and cement matrix with a tailored characterization method. The new method was developed primarily to facilitate epoxy impregnation into the ITZs surrounding a microfiber. In addition, longitudinal section passing through the central axis of the fiber was prepared for ITZ characterization with the help of high precision sawing facility. With the method, the microstructural features of the ITZs between a PVA fiber and cement paste matrices with different w/c ratios were determined by SEM; and the porosity of the ITZs was quantified by backscattered electron (BSE) imaging. The chemical and nanomechanical properties of the ITZ were also characterized by means of nano-indentation and energy-dispersive X-ray spectroscopy (EDS) elemental mapping.

## 2. Materials and tests

### 2.1. Materials

In this study, CEM I 42.5 N Portland cement was used to prepare cement pastes with varying w/c ratios of 0.3, 0.4 and 0.5. The microfiber used to produce the ITZ is a PVA microfiber from Kuraray (Japan) with 1.2% by weight oiling coating, which is commonly used in SHCC and ECC. The nominal diameter of the fiber is 39  $\mu\text{m}$  according to the manufacturer. The oil coating applied on the fiber surface serves as a hydrophobic barrier between the hydrophilic surface of PVA and cement-based matrix. Due to the thin thickness of the coating, the microstructure of the ITZ is not likely to be altered by the coating. Also, since it has been reported that the hydrophobic force has a decay length of only 0.3–1.0 nm [23], the function of the coating is also not expected to affect the properties of the ITZ. Since the distribution caused by the fibers to the matrix is usually not dependent on the composition of the fiber, the findings of the current study should be applicable to cement-based composites incorporating other types of microfibers (e.g., PE microfiber and PP microfiber).

### 2.2. Sample preparation

Two types of specimens were prepared for ITZ characterization as schematically illustrated in Fig. 1. The specimens were prepared from model samples containing only one continuous fiber in its center. To prepare those specimens, a long PVA fiber was first cut into about 150 mm in length and fixed at the center of a prismatic mold, in which fresh cement paste was then pored with sufficient vibration applied during the whole process. A detailed preparation procedure can be found in the Appendix. Specimens with fractured sections were prepared for investigating the morphology of the cross-sections of the ITZ. Specimens with epoxy-impregnated and polished section were prepared for BSE imaging, nanoindentation, and EDS elemental mapping. All the specimens were cured in a climate room (20  $^{\circ}\text{C}$  and  $\geq 98\%$  RH) for a period of 3 months before analysis.

Quantification of the porosity followed the well-established method of using BSE image analysis for pore segmentation. The method usually comprises the following steps: 1) sectioning a specimen to expose the targeted microstructure; 2) impregnating epoxy resin into the pores; 3) grinding and polishing the section; and 4) examining the polished section under BSE. The challenge in using this method to characterize the ITZ surrounding a microfiber is the need to precisely expose the microstructure of the ITZ, which requires making a well-controlled cut in close proximity to the fiber. As the diameter of a microfiber is only a few tens of microns, the positional accuracy of the cutting needs to be in at least micron level. For this reason, an automatic dicing machine was adopted in the current study. The machine is commonly used in the

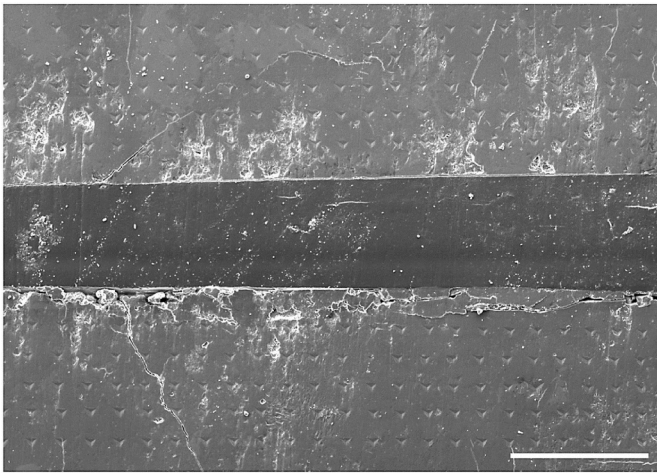


**Fig. 2.** Secondary electron (SE) image of residual indents on a longitudinal cross-section of the ITZ. 5 lines of indents can be found on both sides of the fiber. Scale bar = 50  $\mu\text{m}$ .

semiconductor industry to perform precise cutting of silicon wafers. Further details regarding the preparation procedure can be found in the Appendix. At least 2 specimens were prepared for each w/c ratio for the quantification of porosity in the ITZ.

### 2.3. Tests

Both fractured and polished samples were examined under the BSE detector in an FEI QUANTA FEG 650 environmental SEM in high

vacuum chamber condition. All specimens were coated with a layer of carbon of roughly 10 nm thick before BSE examination. EDS analysis was performed with the same SEM, using a solid-state silicon drift detector (SDD) with a NORVAR window. All analyses were carried out at a working distance of 10 mm and at an accelerating voltage of 15 kV. The take-off angle of the detector was  $35.3^\circ$ . The EDS maps were acquired by using the Pathfinder X-ray Microanalysis Software (Thermo Fisher Scientific) at a resolution of  $1024 \times 682$  pixels over regions of  $512 \mu\text{m}$  by  $341 \mu\text{m}$  (pixel size =  $0.5 \mu\text{m}$ ). The combination of 50  $\mu\text{s}$  dwell time per pixel with an averaging over 50 frames was found to provide good results. The resulting acquisition time of a map is around 30 minutes per area.

Nanoindentation tests were performed by using a G200 Nanoindenter with a continuous stiffness measurements (CSM) module in the ITZ region at both sides of a microfiber. At each side, an array of  $10 \times 30$  indentations at a spacing of  $10 \mu\text{m}$  were performed to cover an area of  $100 \mu\text{m} \times 300 \mu\text{m}$  parallel to the fiber as shown in Fig. 2. The distance between the 1st line of indents and the fiber surface is  $10 \mu\text{m}$ . The results of the 10 lines of indents represent the properties of the ITZ at distances from  $10 \mu\text{m}$  to  $100 \mu\text{m}$ . Each indentation was made to a depth of 500 nm at a strain rate of  $0.05 \text{ s}^{-1}$ . The harmonic frequency and displacement of CSM oscillation are 45 Hz and 2 nm, respectively. The modulus (or hardness) results of each indentation test were determined from the CSM indentation curves by averaging the hardness (or modulus) values between 100 nm and 500 nm indentation depth.

## 3. Results and discussion

### 3.1. Microstructure of the ITZs

Based on our previous investigation [21,22], the microstructure of a

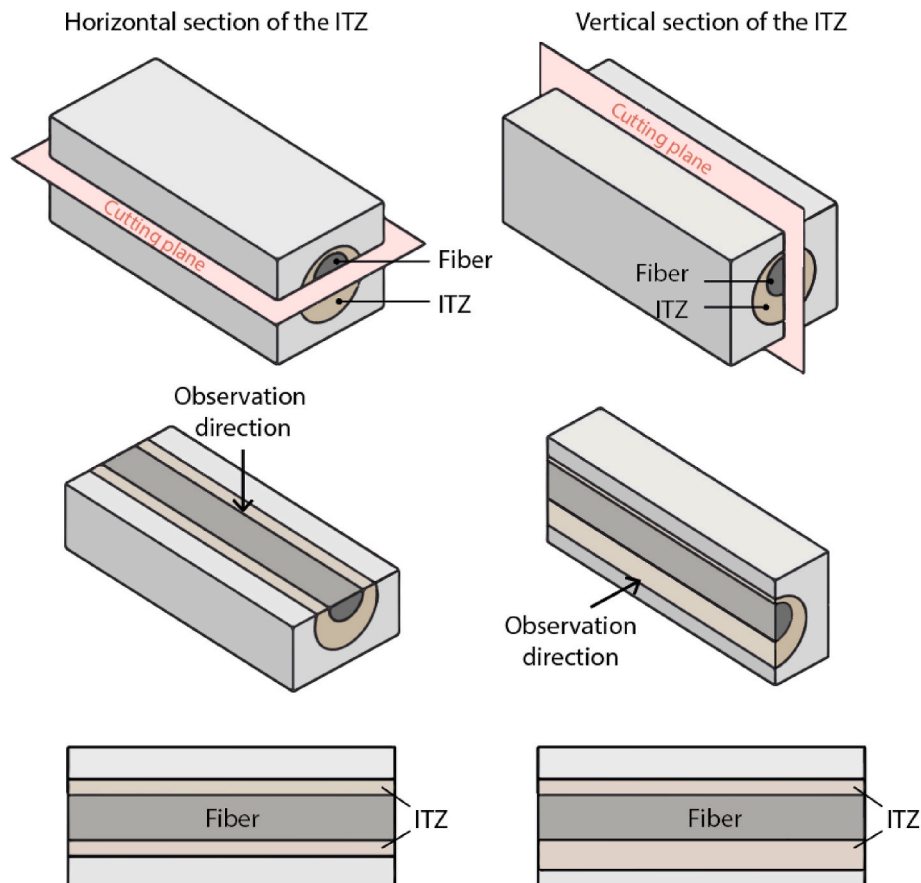


**Fig. 3.** Schematic illustration of horizontal and vertical sections of the ITZ.

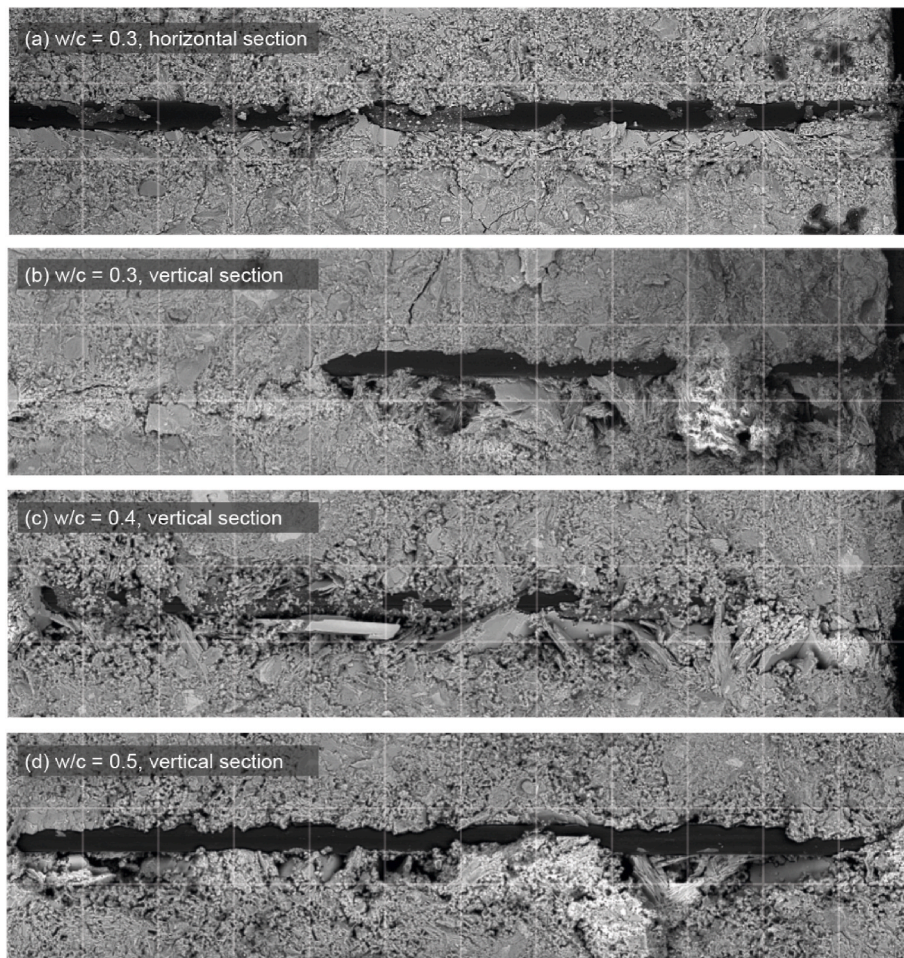


**Fig. 4.** Fracture surface of (a) horizontal section of a specimen at 0.3 w/c ratio; and vertical sections of specimens at w/c ratios of (b) 0.3 (c) 0.4 and (d) 0.5. Each cell in grid is  $100\ \mu\text{m} \times 100\ \mu\text{m}$ .

fiber/matrix ITZ can be highly heterogeneous along its longitudinal direction. It is thus decided to prepare the longitudinal cross-sections of the ITZs to have a panoramic view of a sufficiently long segment of an embedded fiber. However, even with longitudinal sections, the orientation of the section may also be significant. To address this, 2 types of longitudinal sections (*i.e.*, vertical and horizontal section, as schematically illustrated in Fig. 3) were prepared firstly to determine which orientation provides the most suitable perspective for microstructural analysis.

Fig. 4a and b shows the 2 types of longitudinal section under BSE. The images shown are fractured surfaces of specimens with identical w/c ratio. A segment of exposed microfiber with a darker appearance can be seen in the middle of each image. The regions above and below the fiber are longitudinal cross-sections of the ITZ. As can be seen from the images, the microstructures of the ITZ exposed by the 2 types of sections are different. While the horizontal section (Fig. 4a) reveals similar microstructure on both sides of the fiber, the vertical section of the ITZ (Fig. 4b) shows clearly that the microstructure below the fiber is much more heterogeneous than the area above. Pores in the size of several tens of micron can be seen in the ITZ below the fiber, while the upper ITZ is relatively dense without noticeable defects. In addition, some large plate-like crystals can only be found below the fiber. It can be roughly estimated that the largest dimension of some crystals can be around  $100\ \mu\text{m}$ . Fig. 4c and d shows the vertical cross-sections for specimens with 0.4 and 0.5 w/c ratios. As can be seen, the overall features of the microstructure are similar. Areas above the fiber are relatively dense while the areas below the fiber have large pores embedded with plate-

like crystals, possibly calcium hydroxide. Possible mechanisms that give rise to this particular structure will be discussed in the following subsections of the paper. At this point, it can be concluded that only through a vertical section can such a feature of the ITZ be observed. Therefore, all the following characterizations in the current study adopted the vertical section.

Fig. 5 show the BSE images of epoxy impregnated ITZ with polished surface for different w/c ratios. In the BSE images, the brightness of each pixel depends on the mean atomic number of the underlying phases. This allows pores, hydrated phases, and anhydrous phases to be differentiated on the basis of their grayscale. The embedded fiber, which contains mainly the element of carbon, can be easily identified in the middle of each graph as a dark black rectangular. Each specimen has a segment of fiber which is roughly 1.5 mm long. Epoxy filled pores could be seen also in dark black. Each image in Fig. 5 was stitched from at least 30 individual BSE images taken at a magnification of  $3000\times$ . The resulting images have a dimension of roughly  $20,000 \times 10,000$  pixels with a pixel size of 50 nm.

The general features revealed by Fig. 5 are similar to Fig. 4. Irrelevant to the w/c ratio, porosity of the ITZ below a fiber is significantly higher than the ITZ above a fiber. Pores in the size of more than a hundred microns can be observed in all ITZs below a fiber. What is not observed in the fractured surface is that the upper ITZ is also more porous as compared to the bulk matrix further away from the fiber surface. Furthermore, by comparing the individual images of Fig. 5, it can be found that the porosity increases with increasing w/c ratio. While relatively large pores can only be found locally below the fiber at 0.3 w/

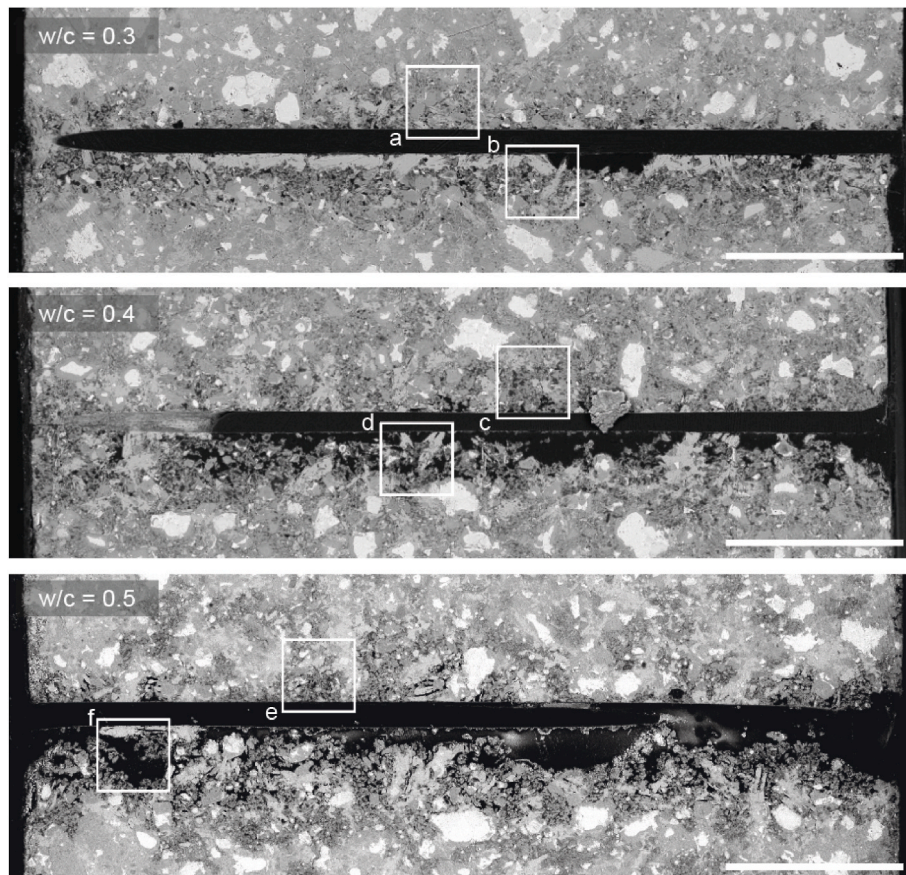


Fig. 5. BSE images of polished sections of the ITZ impregnated with epoxy. Scale bar is 300  $\mu\text{m}$ .

c ratio, a network of connected pores can be seen almost below the entire segment of fiber at 0.4 and 0.5 w/c ratios. The images suggested that a porous transition zone exists around a microfiber. The porosity of the ITZ depends on the w/c ratio, the position of the ITZ with respect to the fiber, and probably also the orientation of the fiber with respect to the casting direction.

Fig. 6 show the close-up views of the ITZ microstructures. The images in the first column are the upper ITZs; and images in the second column show the lower ITZs. The 3 rows correspond to the 3 different w/c ratios. The locations from where the images were cropped are marked in Fig. 5. The most noticeable feature is perhaps the difference in the size of pores between the upper and lower ITZs. While the darker areas (epoxy-impregnated areas) in the upper ITZs are mainly the small gaps between closely packed particles (e.g., B4 and B5 in Fig. 6a, B5 and C5 in Fig. 6c) or the holes inside Hadley grains [24,25] (e.g., upper part of B3 in Fig. 6c, C5 in Fig. 6c), the darker areas in the lower ITZs are large pores in the size of several tens of microns. This suggests that the underlying mechanisms are different for the high porosity at both sides of the fiber. In the upper ITZs, it seems that the wall effect is responsible to the excessive porosity as the presence of many Hadley grains indicates that these areas initially contain mainly small grains. However, in the lower ITZs, it can be noticed that the many particles are not even touching each other, indicating that initially the water was abundant in this area. The precipitation of large calcium hydroxide (CH) crystals in the lower ITZs (C2 in Fig. 6b, D2 in Fig. 6d, D1 in Fig. 6f) also suggests that, below the fiber, there was a region having a significant deficit of cement grain from the beginning of hydration. As the size of the area is beyond 100  $\mu\text{m}$ , the wall effect should not be responsible, for that the porous zone caused by wall effect is usually commensurate with that of the cement grains.

The observed excessive and asymmetric porosity may be attributed

to 3 reasons. Firstly, it has been reported that fiber would interfere with the packing of the particles near them by preventing the filling up of the voids between the particles and the fiber [26,27]. Such a phenomenon is similar to the 'wall' effect but can have an even larger influence depending on the rigidity of the fiber [28]. Since in the current study the fiber was aligned straight and fixed with the mold, it is plausible that the fiber may have loosen the packing of the cement particles around it. Secondly, since in the current study the fiber was horizontally placed, it is possible that the rigidity of fiber in the length direction may have helped shoulder the cement grains above it, leaving more unfilled space underneath. This 'shouldering' effect has been reported to occur with the inclusion of flaky particles, loosening the packing of round particles beneath them [29,30]. Thirdly, in addition to influencing the initial packing of particles, microfibers can also affect the following settlement of fresh mixtures. It is well-known that, during the setting of fresh concrete, water tends to accumulate beneath aggregates, as the solid particles settle down and the water moves upward, a process commonly addressed as micro-bleeding [30,31]. Similarly, water may also accumulate below fibers [32], especially when the density of polymeric fiber is less than that of water, resulting in a locally high w/c ratio as well as high porosity.

### 3.2. Porosity gradient of the ITZs

To further characterize the microstructure around a microfiber, quantification of porosity in the ITZ was carried out by BSE image analysis. Fig. 7 show representative images for porosity quantification before and after grayscale segmentation. In the binary image, the white rectangle in the middle of the image is the embedded fiber. The clustered white pixels represent the pores. The line figures above and next to the binary image show the fraction of white pixels per each vertical and

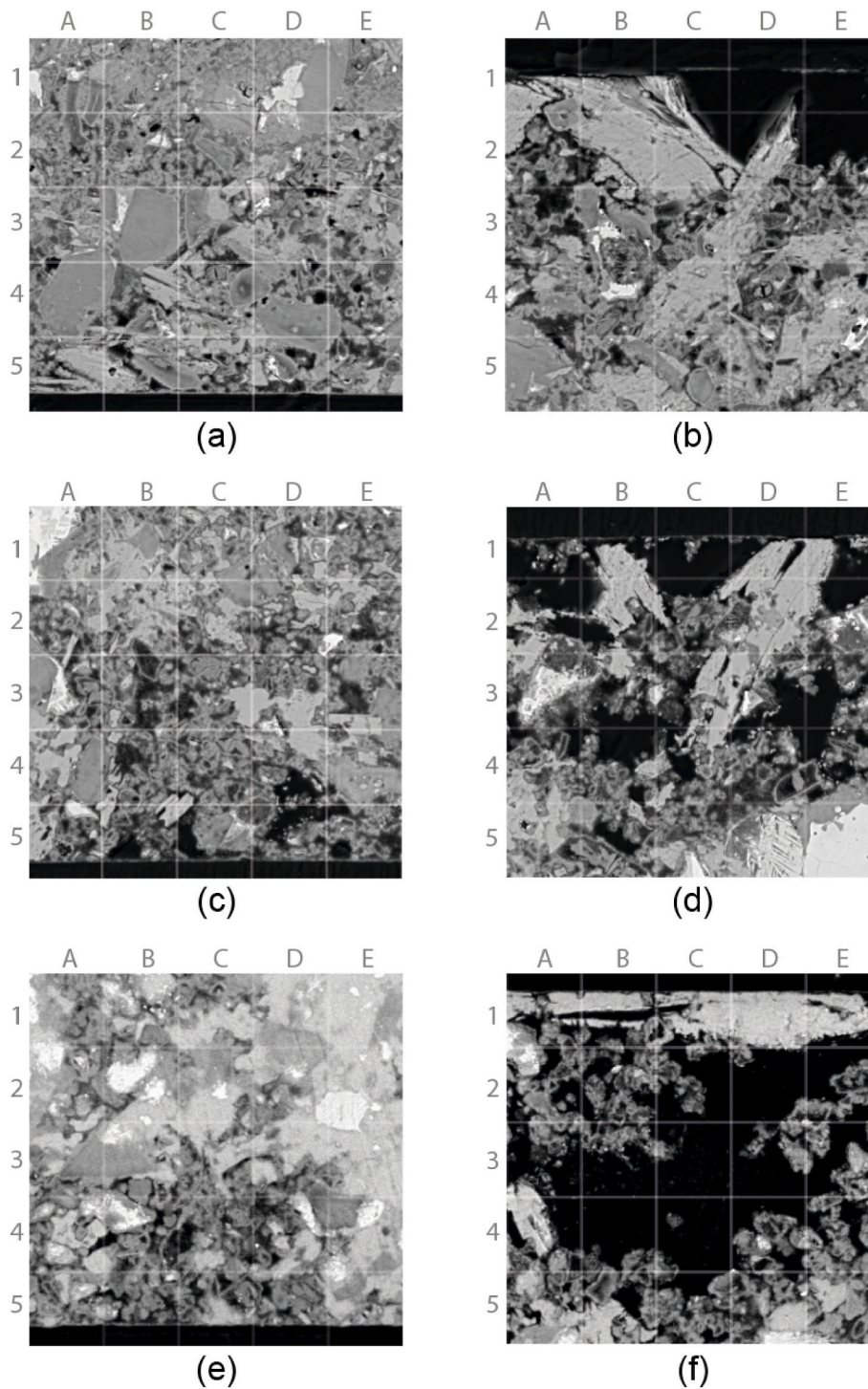


**Fig. 6.** Close-up examinations of the cross-sections of (a, c, e) the upper ITZ and (b, d, f) the lower ITZ. Size of each image is  $100\ \mu\text{m} \times 100\ \mu\text{m}$ . Each cell in grid is  $20\ \mu\text{m} \times 20\ \mu\text{m}$ .

horizontal line, respectively, representing the change of the porosity along the longitudinal and radial directions of a fiber. As can be seen from the line plot on the right of the binary image, the zone in the vicinity of the fiber contains a much higher number of pores as compared to the bulk matrix far away from the fiber, confirming again the existence of a porous transition zone between microfiber and cement matrix. Furthermore, from the line plot above the binary image, it can be found that porosity in the ITZ is not homogeneous along the fiber. Concentration of pores can be seen at some locations, while some areas remain less porous. This reveals that the ITZ between microfiber and cement

paste is highly heterogeneous along its length direction. As a result, characterization of ITZ performed on sections intersecting with fiber at a random angle can lead to errors and uncertainties.

Fig. 8 show the porosity gradient in the ITZs above and below a fiber for different w/c ratios. To ensure reproducibility and the reliability of the results, at least 2 specimens were investigated for each w/c ratio. Fig. 8a presents the results from 2 specimens with the same w/c ratio (i. e., 0.4). The averaged porosity gradients from the 2 specimens were then taken as the characteristic porosity for this w/c ratio. As can be seen, the porosity of ITZ within 0–100  $\mu\text{m}$  is significantly higher than the bulk

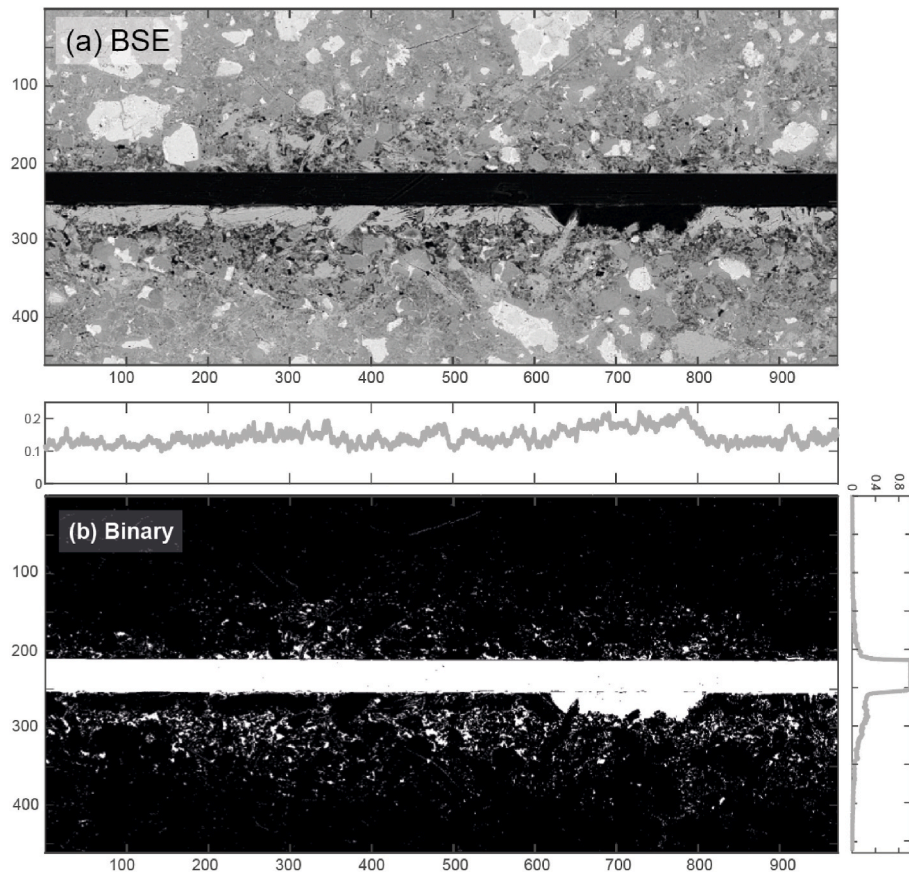


**Fig. 7.** BSE raw image and its binary image after segmentation at a grayscale of 70 ( $w/c = 0.3$ ). Change of fraction of white pixels (pore) to all pixels in each horizontal/vertical line are shown in the line plots above and next to the binary image. The unit for the size of each image is micron.

matrix for all  $w/c$  ratios. The volume fraction of pores decreases with increasing distance from fiber/matrix interface. This suggests that the microstructure of the hydrated cement paste is highly modified in the vicinity of microfibers for all the tested  $w/c$  ratios. By comparing the solid and dash lines in Fig. 8b, the porosity gradients between the upper ITZs and the lower ITZs can be compared. Interestingly, the porosity gradients of the upper ITZ are almost identical for all tested  $w/c$  ratios, while the porosity gradients of the lower ITZ become steeper when the  $w/c$  is higher. When the  $w/c$  ratio is 0.5, the porous zone below the fiber can extend to more than 150  $\mu\text{m}$  away from the fiber surface. This again suggests that the mechanism for the formation of fiber/matrix ITZ is not merely the wall effect. Previous research investigating the thickness of the aggregate/matrix ITZ mostly reports that the more porous zone is only 15–20  $\mu\text{m}$  in width due to the wall effect. Fig. 8c shows the change of normalized porosity at different distances from the fiber/matrix interface for all the  $w/c$  ratios. The curves clearly show that the  $w/c$  ratio has a significant influence on the overall porosity of the ITZ. However, there seems to be a threshold as the porosity gradients appear to be quite similar for  $w/c$  ratios of 0.4 and 0.5.

It should be noted that, as shown in Fig. 8c, the porosity of the ITZ reduces to almost nothing for all  $w/c$  ratios when the distance is far away from the fiber surface, which conflicts with the fact that cement pastes are porous in nature and feature a characteristic porosity at a specific  $w/c$  ratio. This discrepancy is due to the sample preparation procedure as well as the penetration depth of the epoxy. Theoretically, the depth that the epoxy resin can be impregnated into a specimen depends on the porosity of the exposing surface. When there are no open and connected pores, such as in the bulk matrix, the penetration depth is around 20  $\mu\text{m}$ . In the case of the ITZ, epoxy can penetrate much deeper as the pores in the ITZ are larger and more connected. However, during the last 2 steps of the sample preparation procedure (Fig. 1A), a layer of

material roughly 25  $\mu\text{m}$  in thickness was grinded away from the epoxy impregnated surface so to reach the center of the fiber (as illustrated in the Appendix). This means that at this moment only the epoxy in the ITZ can still be seen, the epoxy in the bulk matrix has already been grinded away. Therefore, the porosity of the ITZ measured in the current study can be considered as the excessive porosity as compared to the matrix.

### 3.3. Mechanical and compositional properties of the ITZs

To investigate the effect of having excessive pores on the micro-mechanical and compositional properties of the ITZ, nanoindentation and EDS element mapping were carried out at the interfacial areas. As the scope of the current study is not to establish a relationship between those properties with  $w/c$  ratios, only the results of specimen at a 0.3  $w/c$  are presented (*i.e.*, the same specimen as shown in Fig. 5a). For the nanoindentation test, 2 arrays of 300 indents ( $10 \times 30$ ) covering an area of 100  $\mu\text{m} \times 300 \mu\text{m}$  were probed on both sides of the fiber. Fig. 9 present the results of nanoindentation tests in box plots as a function of the distance between the indents and the fiber/matrix interface. On each box, the central mark (notch) indicates the median, and the bottom and top edges of the box indicate the 25th and 75th percentiles, respectively. The whiskers extend to the most extreme data points excluding the outliers. Outliers are values that are more than 1.5 times the inter-quartile range away from the bottom or top of the box. The average values are superimposed as line plots. The indented areas are marked in Fig. 10, in which the white dots are the locations of indent.

As can be seen from Fig. 9a and b, the mechanical gradients of the lower ITZ and the upper ITZ are markedly different, which is consistent with the findings of our microstructural analysis. While the average modulus of the upper ITZ shows a monotonic increase with distance away from fiber surface, indentation modulus of the lower ITZ firstly

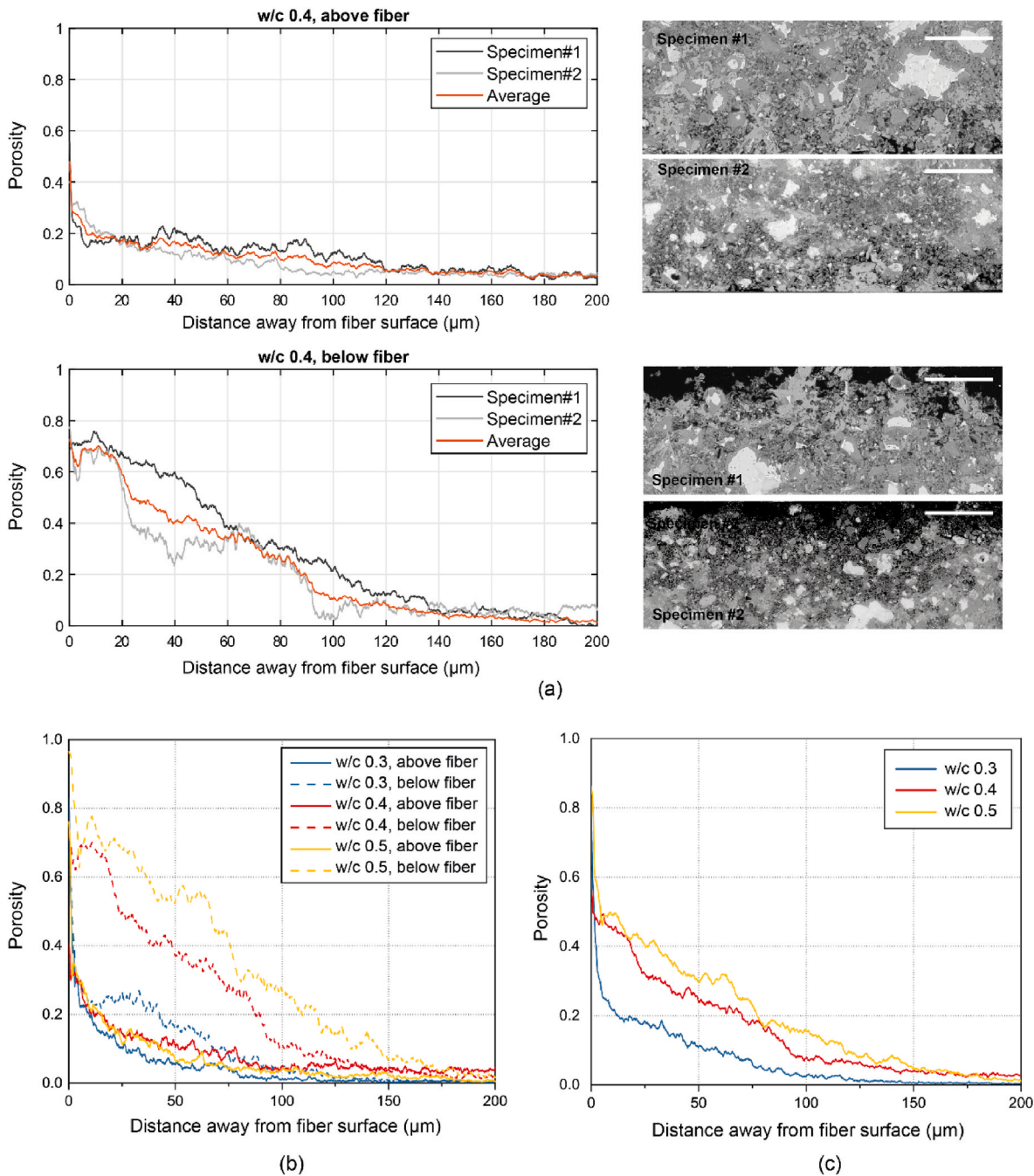


**Fig. 8.** Volume fraction of pores at different distances from the fiber/matrix interface for: (a) 2 specimens with same w/c ratio, (b) averaged upper and lower ITZs for all tested w/c ratios and (c) normalized ITZ for all tested w/c ratios.

decreases until the distance is around 50 μm from fiber and then increases up to the end of the measuring area. An increasing trend of indentation modulus in the ITZ is in general expected, for that the porosity of the ITZ decreases with increasing distance away from fiber as presented in Fig. 8b. The initial decreasing modulus in the lower ITZ is probably because of the CH crystals deposited beneath the fiber. As shown by the elemental mappings in Fig. 10, the top few lines of indents in the lower ITZ were probably probed mainly at the CH phase as these locations are rich in calcium (Fig. 10c) but deficient in silicon (Fig. 10b). The average modulus of the lower ITZ reduces to its lowest at around 50 μm from fiber surface. This is because most of the pores in the lower ITZ are actually below the CH, as shown in Fig. 10a with high intensity in carbon. These areas are exactly 50 μm away from fiber surface. The drop of indentation modulus within 50 μm is probably because that the fiber

surface may have provided more of the nucleation sites to the CH crystals and thus the packing density of the crystals reduces with increasing distance away from fiber surface. Still, a high average modulus does not necessarily mean that the ITZ is strongest when it is close to the fiber surface. Since this area is essentially a mixture of pores and separately deposited CH crystals, the load transfer ability of this part of ITZ is still expected to be limited. This may also be supported by the large scatter of data in this area (the left-most box in Fig. 9a). Since cracks are preferably to initiate from the weakest regions, it is expected this part of the ITZ may still govern the overall strength of the bonding between matrix and fiber.

Fig. 9c shows the behavior of a normalized ITZ by including the indentation results from both sides of the fiber. Though a slight decrease close to the fiber surface can still be noticed, the general trend is that

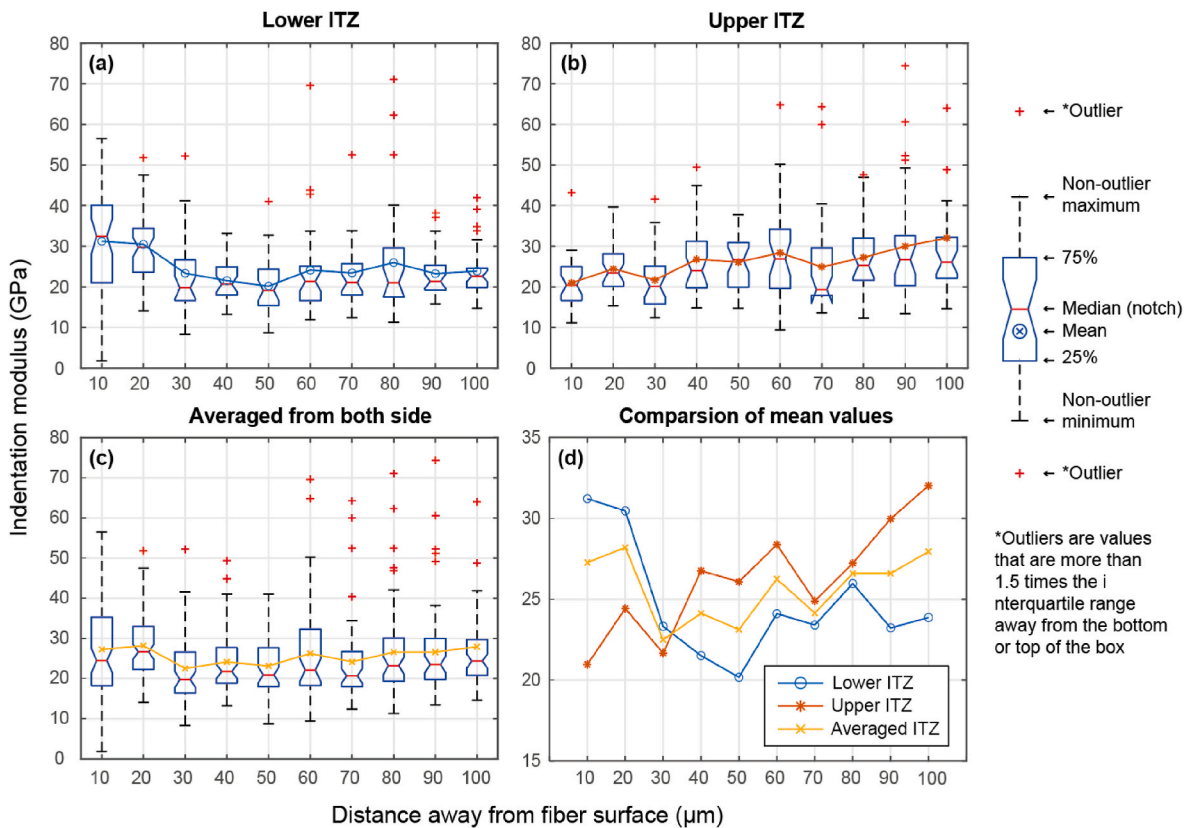


**Fig. 9.** Box plots of modulus gradient ( $w/c = 0.3$ ) for (a) upper ITZ, (b) lower ITZ, and (c) normalized ITZ; and (d) comparison of the mean values. On each box, the central mark (the notch) indicates the median, and the bottom and top edges of the box indicate the 25th and 75th percentiles, respectively. The whiskers extend to the most extreme data points not considered outliers, which are values that are more than 1.5 times the interquartile range away from the bottom or top of the box. The average values are superimposed as line plots.

modulus increases with increasing distance from fiber/matrix interface. Fig. 9d compares the change of average values for the lower, upper, and normalized the ITZ. The difference of modulus between the lower and upper ITZ persists even when the distance is 100  $\mu\text{m}$  away from fiber. The weaker mechanical properties of the lower ITZ should be a direct consequence of having a more porous microstructure. Furthermore, the mapping of silicon (Fig. 10b) may resemble to some extent the initial distribution of cement grains around the fiber. As can be seen from the clusters of bright blue pixels, the presence of a flat surface (upper side of the fiber) enforces order in the packing of cement particles that fall on top. From the line plot on the right of the mapping, it can be seen that this ordering extends for some 20–25  $\mu\text{m}$  diameters away from the flat surface (similar to the wall effect). While on the other side of the fiber, the silicon intensity keeps increasing until it reaches roughly 150  $\mu\text{m}$  away from the fiber surface. This again confirms that a high local porosity underneath the fiber exists.

It should be noted that the micromechanical properties of the ITZ as presented above can only represent the tested areas. It would be fallacious to claim that these properties are general features of the ITZ as a whole, for that the microstructures of the ITZ are significantly heterogeneous along its longitudinal direction as shown in Fig. 5. The question of how large an area should be probed by nanoindentation so to get representative properties of ITZ is beyond the scope of current study. The results from our nanoindentation tests and EDS analysis are presented primarily to demonstrate the different impact of porosity and composition to the micromechanical properties of the ITZ.

### 3.4. Properties of the ITZ in composite specimen

It is noteworthy that the characterizations of the current study were

made on model specimens, in which fibers were aligned straight and fixed rightly with the mold. This arrangement of fiber is indeed unrealistic, since discrete polymeric microfibers are usually bent and orientated randomly in a fiber reinforced cement-based composite. Also, fixed fibers could also disturb the settlement of the fresh mixture and may have complicated the influence of fiber on its surrounding matrix. It is thus possible that the properties of the ITZ measured in the current study may deviate from the properties of ITZ in a composite. To verify this hypothesis, the current study also attempted to characterize the fiber/matrix ITZ from a composite specimen adopting the same mixture composition and the same type of fiber (*i.e.*, a strain-hardening cementitious composite developed previously in the group [33]). This mixture consists of CEM III/B cement and finely ground limestone powder and has a  $w/c$  of 0.4.

Fig. 11 show BSE images and EDS elemental mappings of a random cross-section of a composite specimen. In the BSE images (Fig. 11a and b), fibers can be seen as dark ovals or circular dots as these fibers can intersect with the cutting plan at random angles. Fig. 11b is a zoom-in BSE image of Fig. 11a having one single fiber in its center. By observing the BSE image (Fig. 11b) and the carbon mapping (Fig. 11c), it can be clearly seen that porosity around the fiber was larger than the bulk matrix, and that large pores preferably clustered beneath the fiber. This phenomenon can be further confirmed by the high sulfur intensity beneath the fiber, for that sulfur-containing hydration products such as ettringite and monosulfate preferably form in large pores. In addition, the same area also has a relatively low silicon loading as can be seen from the silicon mapping (Fig. 11e), which again points to an initial loose packing of cement grains. Though this porous zone may indeed look narrower, the features of the ITZ are in line with the observations made with model specimens. Although the preparation method of the

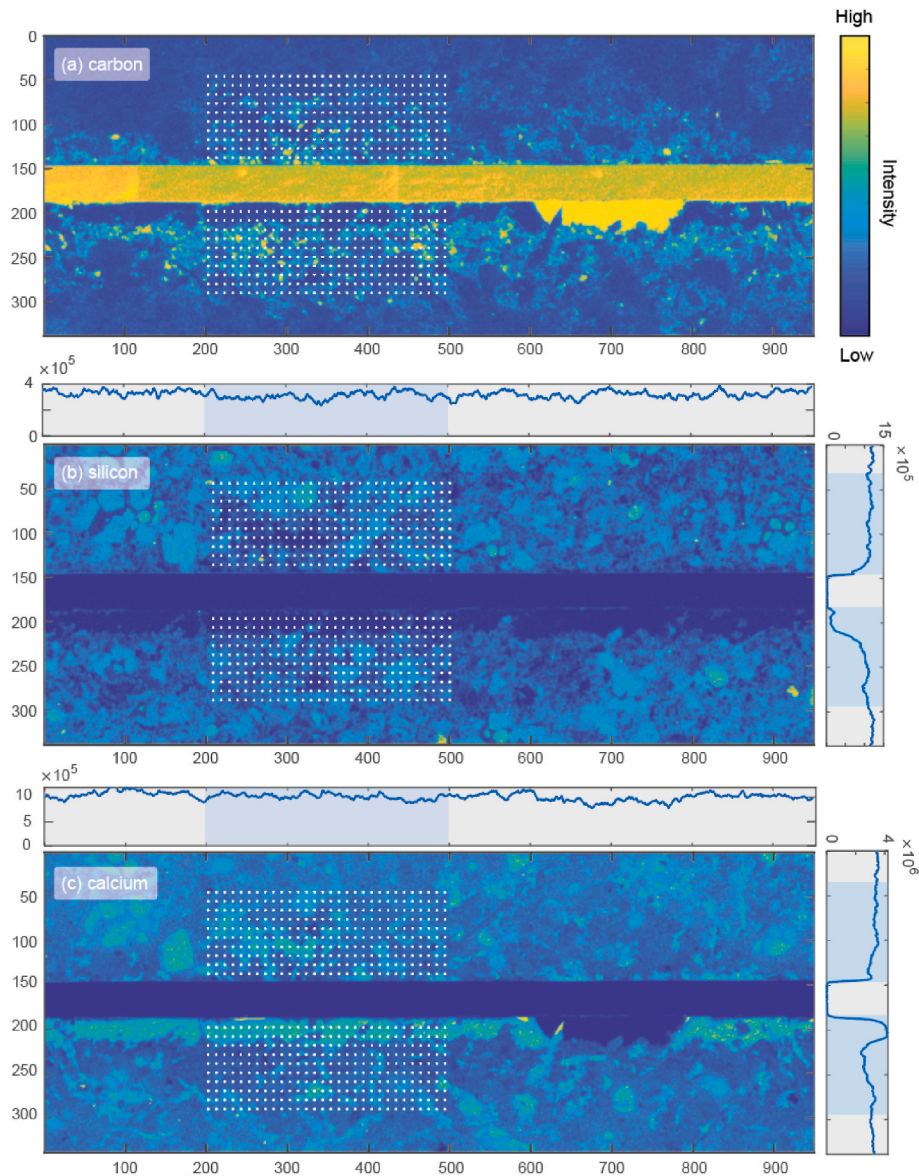


**Fig. 10.** EDS elemental mappings of ITZ ( $w/c = 0.3$ ) for (a) carbon, (b) silicon and (c) calcium. (For interpretation of the references to colour in this figure legend, the reader is referred to the Web version of this article.)

model specimens may have amplified the influence of the fiber on its surrounding matrix to some extent, it can still be concluded that the matrix surrounding a microfiber is porous and that the distribution of porosity is asymmetric. This is attributable to both the shouldering effect of the fiber and the disturbance it creates in the settlement of the fresh mixture below and above the fiber.

Furthermore, it should be noted that previous studies carrying out single fiber pullout tests usually adopt the same sample preparation procedure by which the model specimens were prepared in the current study. The ITZs prepared in these studies should feature the same characteristics as the ITZs presented in the current study. It is thus expected that the fiber/matrix bond properties derived from single fiber pullout tests are also prone to this error caused by the deliberate alignment of fiber.

#### 4. Conclusions

This study investigates the microstructural features of the interfacial transition zone (ITZ) between microfiber and cement pastes with varying water-to-cement ( $w/c$ ) ratios. High resolution BSE images of

fractured and polished ITZ cross-sections were presented and discussed. The porosity, nanomechanical and compositional properties of the fiber/matrix ITZs were also quantified. The main findings of the current study are:

1. The characterization results of the present study suggest the existence of a porous ITZ between the microfiber and cement paste. This porous zone has a thickness of around 100–150  $\mu\text{m}$ . Near the surface of the fiber, the porosity of the ITZ can be even higher than 50%, which might significantly reduce the effective contact area between the fiber and the matrix.
2. The microstructures of the ITZ above and below a microfiber exhibit notable differences. While both ITZ regions near the fiber tend to be more porous than the bulk, the porosity of the lower ITZ is significantly higher than the upper side. This difference can be attributed to several factors, including the effects of the fiber on the initial packing of surrounding cement grains, such as the 'loosening' and 'shouldering' effects, as well as the impact of fiber on the settlement of the fresh mixture, resulting in micro-bleeding.

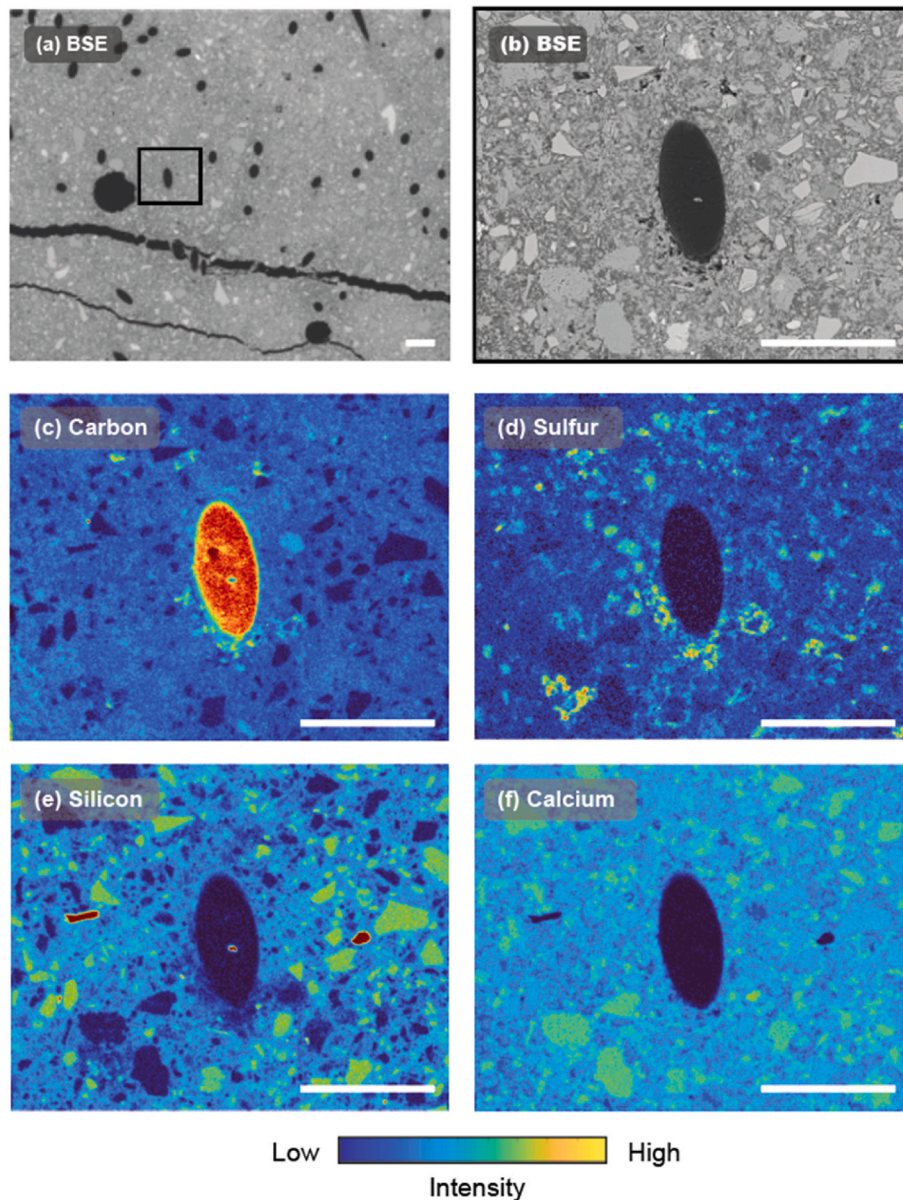


Fig. 11. (a–b) BSE images and (c–e) EDS elemental mappings of a random cross-section of a composite specimen (scale bar, 100  $\mu$ m).

- The quantification of the ITZ porosity shows that the porosity gradients of the upper ITZ are almost constant across all w/c ratios. In contrast, the porosity gradients of the lower ITZ become steeper with higher w/c ratios. Additionally, the bottom side of the ITZ is found to be the preferred site for the precipitation of CH crystals, which again suggests the occurrence of micro-bleeding and locally high w/c ratio.
- Results of nanoindentation tests confirm that mechanical properties of the ITZ are also asymmetric. The upper ITZ has higher mechanical properties than the lower ITZ. Also, it is found that the most inner part of the ITZ does not necessarily have the lowest mechanical properties. The presence of the CH in the vicinity of the fiber can largely influence the local nanomechanical response.
- The characterization of the ITZ between fiber and matrix in a fiber-reinforced composite specimen reveals similar features to those observed in model specimens. The porous zone is thinner, but the matrix surrounding the microfiber is still more porous than the bulk. This finding confirms the presence of a porous ITZ in practical fiber-reinforced materials. Additionally, the porosity distribution is still asymmetric, which indicates that the effects of fiber on the particle

packing and on the fresh mixture settlement observed in model specimens are also present in practical fiber-reinforced composites.

#### Declaration of competing interest

The authors declare that they have no known competing financial interests or personal relationships that could have appeared to influence the work reported in this paper.

#### Data availability

Data will be made available on request.

#### Acknowledgement

Shan He acknowledges the financial support from the MSCA-ITN project SMARTINCS. This project has received funding from the European Union's Horizon 2020 research and innovation programme under the Marie Skłodowska-Curie grant agreement No 860006. Minfei Liang would like to acknowledge the funding supported by China Scholarship

Council under grant number 202007000027.

## Appendix. Detailed Sample Preparation Procedure

Figs. A1 and A2 illustrate the step-by-step sample preparation procedure. To prepare the specimen, a long PVA fiber was first cut into 150 mm in length and taped with a prismatic mold (Fig. A2). After making sure that the fibers were properly aligned, 2 plastic prisms were placed on top and screwed with the mold. This ensures that the fibers will not move with the fresh mixture during casting and can thus remain straight in the hardened specimen, which is crucial for the preparing the longitudinal sections. Next, the mold was filled with fresh cement paste and vibrated for 5 min on a vibration table. The specimens were then covered and allowed to harden at room temperature for 24 h before demolding.

After demolding, the cement paste prism was cured for 3 months in the same climate room (20 °C and  $\geq 98\%$  RH). At the end of curing, hydration of cement paste was stopped by using solvent exchange method with isopropanol. Afterwards, the cement paste prism embedded with one continuous fiber was sliced into thin plate-like specimens with the help of a diamond saw (Steps 1 to 2). The thickness of the specimens is roughly 1.5 mm, and thus each resulting specimen would have a 1.5 mm long segment of fiber embedded in the center. The position of the fiber was then identified with an optical microscope; and a precise cut was made by a dicing saw roughly 5  $\mu\text{m}$  away from the fiber (Steps 2 to 3). This cut should be as close to the embedded fiber as possible so to be within the ITZ, while there should also be some distance between the fiber and the cutting plane to preserve the structure of the ITZ in the observation plane. Fig. A2a shows a top view of a specimen at Sept 4 and Fig. A2b shows the front view. As can be seen Fig. A2b, the cutting plane is only microns away from the top edge of the fiber. And in Fig. A2a, pores in the ITZ around the fiber can be easily seen. Fig. A2c shows the microscopic image under ultraviolet (UV) light of a specimen after being impregnated with a fluorescent resin. The specimen has an embedded fiber aligning vertically in the middle of the specimen. As can be seen, the epoxy successfully impregnated into the pores near the fiber. Fig. A2d is a BSE image of a zoom-in area, showing that the relatively wide porous region can be roughly a few hundred microns wide.

The next step of the preparation is to progressively grind away excessive epoxy at the surface and to reach the cross-sectional plane of the ITZ. The grinding process stopped exactly when the grinding surface reached the center of the fiber (Steps 5 to 6). The last step is to carefully polish the surface for optimum imaging under the BSE. Fine grinding and polishing were then performed by using a LaboPol-60 grinding/polishing machine from Struers (Denmark). Grinding was carried out by using 4000 grit abrasive papers and the polishing was performed by using a synthetic silk polishing cloth (MD-Dac from Struers) charged with 3  $\mu\text{m}$  and 1  $\mu\text{m}$  diamond paste for two 5-min sessions. An oil-based lubricant (DP-Lubricant Brown from Struers) was used to dissipate any heat built-up. Between each grinding/polishing interval, the sample was immersed in an ultrasonic bath for 30 s to remove debris from the surface.

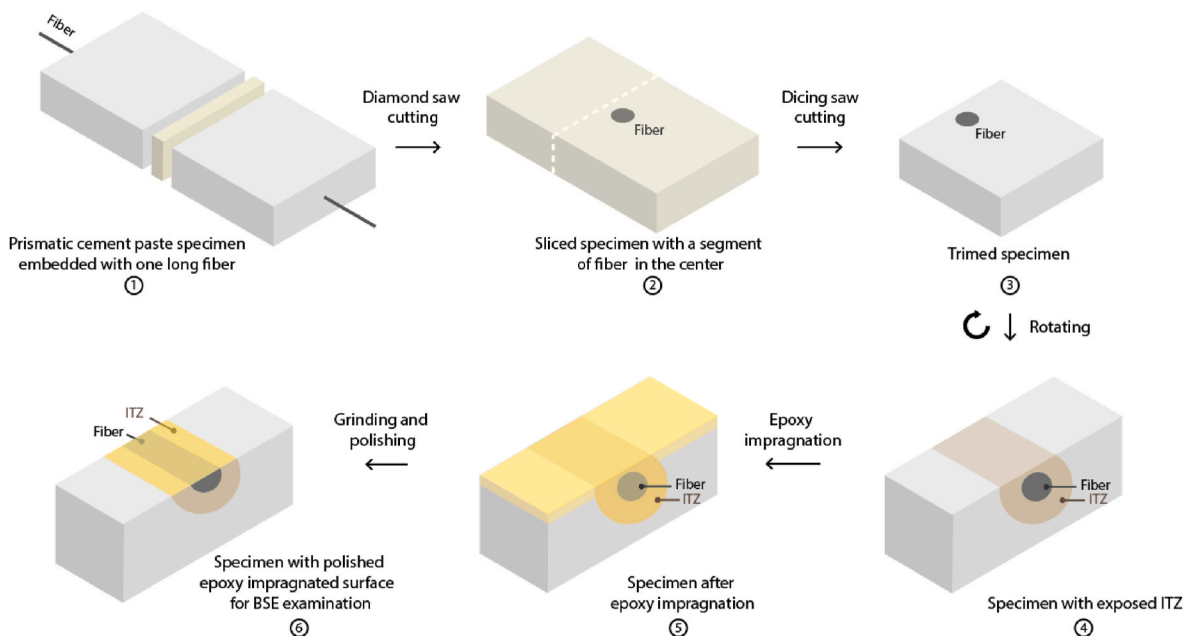


Fig. A1. Schematic illustrations of the sample preparation procedure

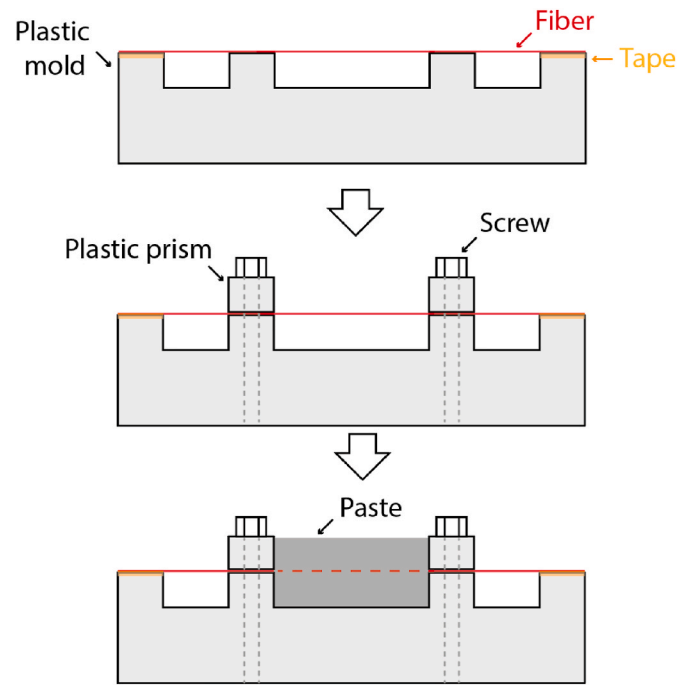


Fig. A2. Schematic illustrations of the procedure to prepare fiber-embedded cement paste specimen.

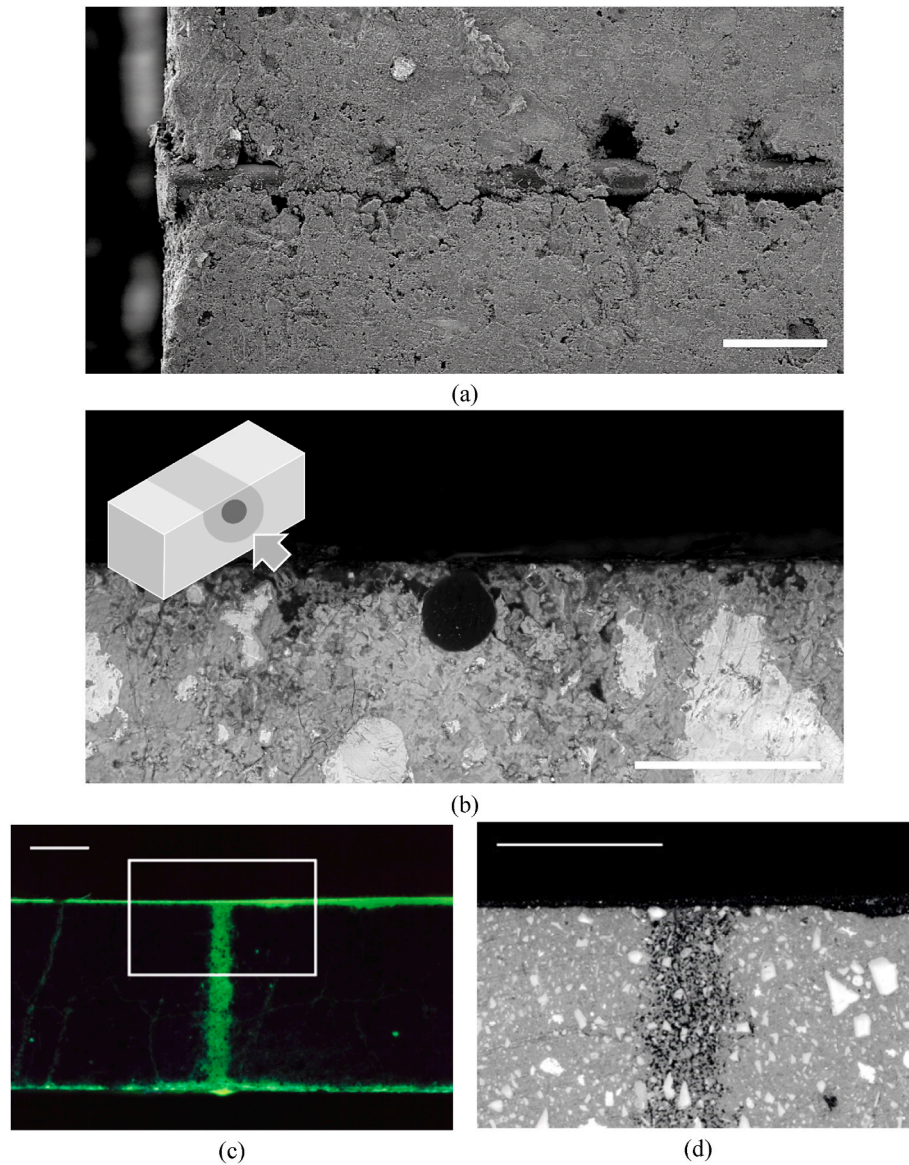


Fig. A3. Emission microscope image of the specimen with exposed ITZ before epoxy impregnation at Step 4: (a) top view (scale bar, 100  $\mu\text{m}$ ) and (b) front view (scale bar, 100  $\mu\text{m}$ ); and (c) fluorescence light micrograph (scale bar, 500  $\mu\text{m}$ ) and (d) BSE image of the specimen after epoxy impregnation at Step 5 (scale bar, 500  $\mu\text{m}$ ).

## References

- [1] V.C. Li, C.K.Y. Leung, Steady state and multiple cracking of short random fiber composites, *J. Eng. Mech.* 118 (1992) 2246–2264, [https://doi.org/10.1061/\(ASCE\)0733-9399\(1992\)118:11\(2246\)](https://doi.org/10.1061/(ASCE)0733-9399(1992)118:11(2246)).
- [2] H. Tanano, Y. Masuda, Characteristics and Performance Evaluation Methods of Continuous Fiber Bars—State of the Art Studies on Fire Properties and Durability of Continuous Fiber Reinforced Concrete in Japan, vol. 188, Special Publication, 1999, pp. 523–534, <https://doi.org/10.14359/5651>.
- [3] A. Peled, S. Sueki, B. Mobasher, Bonding in fabric–cement systems: effects of fabrication methods, *Cement Concr. Res.* 36 (2006) 1661–1671, <https://doi.org/10.1016/J.CEMCONRES.2006.05.009>.
- [4] V.C. Li, D.K. Mishra, H.-C. Wu, Matrix design for pseudo-strain-hardening fibre reinforced cementitious composites, *Mater. Struct.* 28 (10) (1995) 586–595, <https://doi.org/10.1007/BF02473191>, 28 (1995).
- [5] S. He, E.H. Yang, Non-normal distribution of residual flexural strengths of steel fiber reinforced concretes and its impacts on design and conformity assessment, *Cem. Concr. Compos.* 123 (2021), 104207, <https://doi.org/10.1016/J.CEMCONCOMP.2021.104207>.
- [6] R. Ranade, V.C. Li, W.F. Heard, B.A. Williams, Impact resistance of high strength-high ductility concrete, *Cement Concr. Res.* 98 (2017) 24–35, <https://doi.org/10.1016/J.CEMCONRES.2017.03.013>.
- [7] Y. Yang, M.D. Lepech, E.H. Yang, V.C. Li, Autogenous healing of engineered cementitious composites under wet–dry cycles, *Cement Concr. Res.* 39 (2009) 382–390, <https://doi.org/10.1016/J.CEMCONRES.2009.01.013>.
- [8] S.C. Paul, G.P.A.G. van Zijl, B. Šavija, Effect of fibers on durability of concrete: a practical review, *Materials* 13 (2020) 4562, <https://doi.org/10.3390/MA13204562>, 13 (2020) 4562.
- [9] V.C. Li, Engineered Cementitious Composites (ECC), *Engineered Cementitious Composites, ECC*, 2019, <https://doi.org/10.1007/978-3-662-58438-5>.
- [10] V.C. Li, C. Wu, S. Wang, A. Ogawa, T. Saito, Interface tailoring for strain-hardening polyvinyl alcohol-engineered cementitious composite (PVA-ECC), *Materials Journal* 99 (2002) 463–472, <https://doi.org/10.14359/12325>.
- [11] V.C. Li, Tailoring ECC for special attributes: a review, *Int J Concr Struct Mater* 6 (2012) 135–144, <https://doi.org/10.1007/S40069-012-0018-8>.
- [12] Y.W. Chan, V.C. Li, Effects of transition zone densification on fiber/cement paste bond strength improvement, *Adv. Cement Base Mater.* 5 (1997) 8–17, [https://doi.org/10.1016/S1065-7355\(97\)90010-9](https://doi.org/10.1016/S1065-7355(97)90010-9).
- [13] Y. Gao, G. de Schutter, G. Ye, Z. Tan, K. Wu, The ITZ microstructure, thickness and porosity in blended cementitious composite: effects of curing age, water to binder ratio and aggregate content, *Compos. B Eng.* 60 (2014) 1–13, <https://doi.org/10.1016/J.COMPOSITESB.2013.12.021>.
- [14] K.L. Scrivener, A.K. Crumie, P. Laugesen, The interfacial transition zone (ITZ) between cement paste and aggregate in concrete, *Interface Sci.* 12 (4) (2004) 411–421, <https://doi.org/10.1023/B:INTS.0000042339.92990.4C>, 12 (2004).

- [15] J.P. Ollivier, J.C. Maso, B. Bourdette, Interfacial transition zone in concrete, *Adv. Cement Base Mater.* 2 (1995) 30–38, [https://doi.org/10.1016/1065-7355\(95\)90037-3](https://doi.org/10.1016/1065-7355(95)90037-3).
- [16] L. Xu, F. Deng, Y. Chi, Nano-mechanical behavior of the interfacial transition zone between steel-polypropylene fiber and cement paste, *Construct. Build. Mater.* 145 (2017) 619–638, <https://doi.org/10.1016/j.conbuildmat.2017.04.035>.
- [17] G. Tiberti, F. Minelli, G. Plizzari, Cracking behavior in reinforced concrete members with steel fibers: a comprehensive experimental study, *Cement Concr. Res.* 68 (2015) 24–34, <https://doi.org/10.1016/j.cemconres.2014.10.011>.
- [18] D.J. Pinchin, D. Tabor, Interfacial phenomena in steel fibre reinforced cement I: structure and strength of interfacial region, *Cement Concr. Res.* 8 (1978) 15–24, [https://doi.org/10.1016/0008-8846\(78\)90054-6](https://doi.org/10.1016/0008-8846(78)90054-6).
- [19] P.J.M. Monteiro, J.C. Maso, J.P. Ollivier, The aggregate-mortar interface, *Cem. & Cone. Res.* 15 (1985) 953–958, [https://doi.org/10.1016/0008-8846\(85\)90084-5](https://doi.org/10.1016/0008-8846(85)90084-5).
- [20] K.L. Scrivener, E.M. Gartner, Microstructural gradients in cement paste around aggregate particles, *MRS Online Proc. Libr.* 114 (1) (1987) 77–85, <https://doi.org/10.1557/PROC-114-77>, 114 (2011).
- [21] S. He, Z. Li, E.-H. Yang, Quantitative characterization of anisotropic properties of the interfacial transition zone (ITZ) between microfiber and cement paste, *Cement Concr. Res.* 122 (2019) 136–146, <https://doi.org/10.1016/j.cemconres.2019.05.007>.
- [22] S. He, E.-H. Yang, Strategic strengthening of the interfacial transition zone (ITZ) between microfiber and cement paste matrix with carbon nanofibers (CNFs), *Cem. Concr. Compos.* 119 (2021), 104019, <https://doi.org/10.1016/j.cemconcomp.2021.104019>.
- [23] W.A. Ducker, D. Mastropietro, Forces between extended hydrophobic solids: is there a long-range hydrophobic force? *Curr. Opin. Colloid Interface Sci.* 22 (2016) 51–58, <https://doi.org/10.1016/j.cocis.2016.02.006>.
- [24] D. Hadley, *The Nature of the Paste-Aggregate Interface*, Purdue University, 1972.
- [25] M.K. Head, H.S. Wong, N.R. Buenfeld, Characterisation of ‘Hadley’ grains by confocal microscopy, *Cement Concr. Res.* 36 (2006) 1483–1489, <https://doi.org/10.1016/j.cemconres.2005.12.020>.
- [26] S.H. Chu, Y. Jiang, A.K.H. Kwan, Effect of rigid fibres on aggregate packing, *Construct. Build. Mater.* 224 (2019) 326–335, <https://doi.org/10.1016/j.conbuildmat.2019.07.072>.
- [27] C. Gong, L. Kang, L. Liu, M. Lei, W. Ding, Z. Yang, A novel prediction model of packing density for single and hybrid steel fiber-aggregate mixtures, *Powder Technol.* 418 (2023), 118295, <https://doi.org/10.1016/j.powtec.2023.118295>.
- [28] L.G. Li, S.H. Chu, K.L. Zeng, J. Zhu, A.K.H. Kwan, Roles of water film thickness and fibre factor in workability of polypropylene fibre reinforced mortar, *Cem. Concr. Compos.* 93 (2018) 196–204, <https://doi.org/10.1016/j.cemconcomp.2018.07.014>.
- [29] J.C. Santamarina, G.C. Cho, Soil behaviour: the role of particle shape, in: *Advances in Geotechnical Engineering: the Skempton Conference, 2004*, pp. 604–617, <https://doi.org/10.1680/aigev1.32644.0035>.
- [30] M. Guimaraes, *Crushed Stone Fines and Ion Removal from Clay Slurries-Fundamental Studies*, Georgia Institute of Technology, 2002. <https://smartech.gatech.edu/handle/1853/20493>. (Accessed 20 September 2022).
- [31] K. Lyu, E.J. Garboczi, W. She, C. Miao, The effect of rough vs. smooth aggregate surfaces on the characteristics of the interfacial transition zone, *Cem. Concr. Compos.* 99 (2019) 49–61, <https://doi.org/10.1016/j.cemconcomp.2019.03.001>.
- [32] H. Li, L. Li, L. Li, J. Zhou, R. Mu, M. Xu, Influence of fiber orientation on the microstructures of interfacial transition zones and pull-out behavior of steel fiber in cementitious composites, *Cem. Concr. Compos.* 128 (2022), 104459, <https://doi.org/10.1016/j.cemconcomp.2022.104459>.
- [33] S. He, S. Zhang, M. Luković, E. Schlangen, Effects of bacteria-embedded polylactic acid (PLA) capsules on fracture properties of strain hardening cementitious composite (SHCC), *Eng. Fract. Mech.* 268 (2022), 108480, <https://doi.org/10.1016/j.engfracmech.2022.108480>.